Partially coherent radially polarized fractional vortex beam

Jun Zeng,[1,2] **Chunhao Liang,**[3] **Haiyun Wang,**[1] **Fei Wang,**[1] **Chengliang Zhao,**[1,4] **Greg Gbur,**[2,5] **and Yangjian Cai**[1,3,6]

[1] *School of Physical Science and Technology & Collaborative Innovation Center of Suzhou Nano Science and Technology, Soochow University, Suzhou 215006, China*
[2] *Department of Physics and Optical Science, University of North Carolina at Charlotte, Charlotte, North Carolina 28223, USA*
[3] *Shandong Provincial Engineering and Technical Center of Light Manipulations & Shandong Provincial Key Laboratory of Optics and Photonic Device, School of Physics and Electronics, School of Physics and Electronics, Shandong Normal University, Jinan 250014, China*
[4] *zhaochengliang@suda.edu.cn*
[5] *gjgbur@uncc.edu*
[6] *yangjiancai@suda.edu.cn*

Abstract: A new kind of partially coherent vector beam, named a partially coherent radially polarized fractional vortex (PCRPFV) beam, is introduced as a natural extension of the recently introduced scalar partially coherent fractional vortex beams [Zeng et al., Opt. Express, **26**, 26830 (2018)]. Realizability conditions and propagation formulas for a PCRPFV beam are derived. Statistical properties of a focused PCRPFV beam, such as average intensity, degree of polarization, state of polarization and cross-spectral density matrix, are illustrated in detail and compared with that of a partially coherent radially polarized integer vortex beam and a scalar partially coherent fractional vortex beam. It is found that the statistical properties of a PCRPFV beam are qualitatively different from these simpler beam classes and are strongly determined by the vortex phase (i.e., fractional topological charge) and initial coherence width. We demonstrate experimental generation of PCRPFV beams and confirm their behavior. Our results will be useful for the rotating and trapping of particles, the detection of phase objects, and polarization lidar systems.

1. Introduction

Polarization is one of the fundamental properties of a light beam. The vector nature of light and its interactions with matter make possible many optical system designs and optical devices that are unachievable with scalar beams. Vector beams can be separated into those with a spatially uniform state of polarization (SOP) and those with a spatially non-uniform SOP [1]. An archetype of beams with non-uniform SOP, radially polarized beams have found advantages in optical trapping, laser machining, material processing, electron acceleration, microscopy, lithography, optical data storage, plasmonic focusing and super-resolution imaging, due to their unique and interesting focusing properties [1–4]. In high numerical aperture focusing, a radially polarized field leads to a strong longitudinal electric field component at the focus and it can be focused to a spot size significantly smaller than is possible for linear polarization.

In past decades, the coherence and polarization of beams were always studied separately. In 2003, however, Wolf formulated an unified theory of coherence and polarization, which indicates that these properties are interrelated and should be considered together [5]. Wolf characterized the degree of coherence using the visibility of interference fringes, which depends on both statistics and polarization. Meanwhile, Tervo *et al.* gave another definition of the degree of coherence of a partially coherent vector beam, which can be used to analyze the statistical properties of a

partially coherent vector beam [6]. After that, it was found that modulating the coherence and polarization properties of a partially coherent vector beam is useful for beam shaping [7], ghost imaging [8,9] and reducing turbulence effects [10,11]. Thus, more and more attention has been paid to partially coherent vector beams [12–23].

It is generally thought that the degree of polarization (DOP) and SOP of a radially polarized beam are invariant as the beam propagates in free space. However, the above theoretical and experimental studies have shown that a partially coherent radially polarized beam exhibits unique statistical and propagation properties. For example, during propagation in free space, a partially coherent radially polarized beam becomes depolarized (i.e., the DOP decreases on propagation), while its SOP remains radially polarized [20]. Furthermore, modulating the spatial coherence width and correlation function results in beam shaping and can be used to flexibly shape the focused beam spot of the partially coherent radially polarized beam from a Gaussian profile (i.e., bright spot) to a hollow profile (i.e, dark spot) [21,22]. The bright spot required for trapping particles with refractive indices higher than that of the background and the dark spot required for trapping particles with refractive indices less than that of the background can be formed, respectively, in one optical trap system [2]. A partially coherent radially polarized beam can effectively reduce scintillation in turbulence compared to a linearly polarized partially coherent beam [23].

In addition to polarization and coherence, phase is another fundamental property of a light beam. Recently, considerable attention has been paid to beams which possess a vortex phase because of their great potential application in optical micromanipulations, free-space optical communications, optical trapping, optical imaging, deep microstructure topography characterization and optical measurement [24–31]. Quite recently, Fang *et al.* implemented orbital angular momentum holography for high security encryption by using a vortex beam [32]. The vortex phase is determined by the topological charge (TC) carried by a vortex beam [33,34]. The introduction of vortex phase can not only improve the image resolution [35], but also further reduce turbulence effects [36]. In addition, a partially coherent beam embedded with a vortex phase has unique physical effects that beams without a vortex phase do not possess, such as coherence singularities [37,38], which can be used for optical measurement [39]. In 2016, Guo *et al.* introduced a vortex phase into a partially coherent radially polarized beam, and found that the vortex phase plays a role in resisting the coherence-induced degradation of the intensity distribution and the coherence-induced depolarization [40].

The aforementioned research considers beams with an integer topological charge, and the topological charge of a vortex beam is always constrained to be integer valued. However, it is possible to design optical elements that would in principle produce a beam with a fractional TC, and the resulting fields possess some special optical properties that are quiet different from integer vortex beams [41–43]. For example, a fractional vortex beam possesses radial lines of low intensity in its annular intensity ring and the phase changes rapidly at this radial gap; in addition, beams of light with orbital angular momentum such as Laguerre-Gaussian beams are characterized by a central phase singularity, and the number of phase singularities carried by a fractional vortex beam is no longer simply equal to the value of TC, but is determined by the relationship between the value of carried TC and the nearest half-integer. In contrast with an integer vortex beam, a fractional vortex beam has unique advantages in practical applications. For example, the fractional vortex beam's radial opening gap in the intensity can be used for guiding and transporting particles [44] as well as optical sorting [45]. Due to its asymmetric intensity profile, the fractional vortex beam can be applied to achieve anisotropic edge enhancement in imaging [46]. Based on its fractional orbital angular momentum, the fractional vortex beam can be used to increase the degree of entanglement of photons in quantum information processing [47]. Therefore, numerous efforts on a fractional vortex beam have been reported in the last two years [48–54].

The advantages of fractional vortex beams can be combined with the advantages of partial coherence and those of vector beams. In 2018, Zeng *et al.* [53] first introduced a fractional vortex phase into a partially coherent scalar beam and found that the partially coherent fractional vortex beam exhibits unique propagation properties from those of a partially coherent integer vortex beam.

Recently, Gu *et al.* used the collinear superposition principle to generate a fractional ellipse perfect vector beam [54], however, the light source they used was fully coherent. In addition, the selected beam model (note that the perfect beam model can only be generated in the focal field) determines that they can only study its focal field characteristics, but not its propagation characteristics, in general, the study of such beams is very limited. A combination of fractional vortices, partially coherence, and vector effects has not yet been done.

In this paper, we introduce a new kind of partially coherent vector beam called a partially coherent radially polarized fractional vortex (PCRPFV) beam, and discuss its realizability and beam conditions. In particular, we analyze the average intensity, degree of polarization, state of polarization and cross-spectral density matrix of a PCRPFV beam on propagation in detail, and we also report experimental generation of such beams. We discuss unusual effects associated with such beams and their possible uses.

2. Theoretical model and realizability conditions for a PCRPFV beam

According to the unified theory of optical coherence and polarization [55], the statistical properties of a partially coherent vector beam-like field, propagating along the z-axis, can be characterized by the cross-spectral density (CSD) matrix $\overleftrightarrow{W}(\boldsymbol{r}_1, \boldsymbol{r}_2)$ in the space-frequency domain, where $\boldsymbol{r}_1$ and $\boldsymbol{r}_2$ are two arbitrary position vectors in a plane of constant z, perpendicular to the propagation axis. In the source plane ($z = 0$), the elements of its CSD matrix are expressed as

$$W_{\alpha\beta}(\boldsymbol{r}_1, \boldsymbol{r}_2) = \left\langle E_\alpha^*(\boldsymbol{r}_1) E_\beta(\boldsymbol{r}_2) \right\rangle, (\alpha, \beta = x, y), \tag{1}$$

where $E_x(\boldsymbol{r})$ and $E_y(\boldsymbol{r})$ represent two orthogonal stochastic electric field components along the x and y axis, respectively. The asterisks represent the complex conjugate and the angular brackets denote an ensemble average.

As a natural extension of a scalar partially coherent vortex beam with tunable topological charge [53], we define the elements of the CSD matrix of a partially coherent radially polarized beam with Gaussian correlation function and vortex phase $\exp(il\varphi)$ in the source plane ($z = 0$) in following form

$$W_{\alpha\beta}(\boldsymbol{r}_1, \boldsymbol{r}_2) = \frac{\alpha\beta}{w_0^2} \exp(-\frac{r_1^2 + r_2^2}{w_0^2}) \exp[-il(\varphi_1 - \varphi_2)]\mu_{\alpha\beta}(\boldsymbol{r}_1 - \boldsymbol{r}_2), (\alpha, \beta = x, y), \tag{2}$$

with

$$\mu_{\alpha\beta}(\boldsymbol{r}_1 - \boldsymbol{r}_2) = B_{\alpha\beta} \exp\left[-\frac{(\boldsymbol{r}_1 - \boldsymbol{r}_2)^2}{2\sigma_{\alpha\beta}^2}\right], (\alpha, \beta = x, y), \tag{3}$$

where w_0 is the beam width of the source, $\sigma_{\alpha\beta}$ are the coherence widths of the correlation functions with $\alpha - \beta$ components. The quantity l denotes the TC and can be determined by a path integral of the gradient of the wavefield phase $\psi(\mathbf{r})$ with the following expression [33]

$$l = \frac{1}{2\pi} \oint_C \nabla\psi(\mathbf{r}) \cdot d\boldsymbol{r}, \tag{4}$$

where C denotes a closed path around the singularity and $d\boldsymbol{r}$ represents an infinitesmal vector path element. Originally, the definition of l was only for the case where the TC is an integer, but

in 2004 Berry suggested how it could be formally introduced for non-integer cases [41]. The quantity φ is the azimuthal (angle) coordinate, $B_{\alpha\beta} = |B_{\alpha\beta}| \exp(i\phi_{\alpha\beta})$ is the complex correlation coefficient between the α and β components of the electric field with $\phi_{\alpha\beta}$ being the phase difference. By choosing a fractional value of l, the beam source whose CSD matrix is given by Eq. (2) is termed a PCRPFV beam. When the value of l is equal to a non-zero integer, the beam source reduces to a partially coherent radially polarized integer vortex beam [40]. In particular, when $l = 0$, the beam source reduces to a partially coherent radially polarized beam [20,22,23].

A fundamental difference between optical beam modes with integer TCs, and beams with fractional TCs is that the latter are not self-similar on propagation, and the propagation dynamics are therefore more complex. For integer l values, the phase fronts for a given phase $\exp(il\varphi)$ comprise l intertwined helical surfaces giving a screw dislocation along the beam axis, and a resulting annular intensity cross-section. However, for non-integer l values, there is a phase discontinuity, in our case, radially along the $\varphi = 0$ direction, which on propagation gives rise to a line of low intensity.

Now, let us discuss the realizability conditions of a PCRPFV beam, as not every choice of parameters in Eqs. (2) and (3) can be physically achieved. Firstly, the CSD matrix must be Hermitian conjugate, as seen from its definition shown in Eq. (1) [56]. Hence, the following conditions must be met

$$|B_{\alpha\beta}| = 1, \phi_{\alpha\beta} = 0, (\alpha = \beta),$$
$$|B_{\alpha\beta}| \leq 1, |B_{xy}| = |B_{yx}|, \phi_{xy} = \phi_{yx}, (\alpha \neq \beta),$$
$$\sigma_{xy} = \sigma_{yx}. \tag{5}$$

Secondly, to be a physically realizable CSD matrix [57], it is sufficient to have a representation of the following integral form

$$W_{\alpha\beta}(\boldsymbol{r}_1, \boldsymbol{r}_2) = \int p_{\alpha\beta}(\boldsymbol{v}) H_\alpha^*(\boldsymbol{r}_1, \boldsymbol{v}) H_\beta(\boldsymbol{r}_2, \boldsymbol{v}) \, \mathrm{d}^2\boldsymbol{v}, \tag{6}$$

where $H_x(\boldsymbol{r}, \boldsymbol{v})$ and $H_y(\boldsymbol{r}, \boldsymbol{v})$ are two arbitrary functions, and $p_{\alpha\beta}(\boldsymbol{v})$ are the elements of the following weighting matrix

$$p_{\alpha\beta}(\boldsymbol{v}) = \begin{pmatrix} p_{xx}(\boldsymbol{v}) & p_{xy}(\boldsymbol{v}) \\ p_{yx}(\boldsymbol{v}) & p_{yy}(\boldsymbol{v}) \end{pmatrix}. \tag{7}$$

The elements of the weighting matrix should satisfy the non-negative definiteness conditions [57]

$$p_{xx}(\boldsymbol{v}) \geq 0, \quad p_{yy}(\boldsymbol{v}) \geq 0, \quad p_{xx}(\boldsymbol{v})p_{yy}(\boldsymbol{v}) - p_{xy}(\boldsymbol{v})p_{yx}(\boldsymbol{v}) \geq 0. \tag{8}$$

The functions $H_x(\boldsymbol{r}, \boldsymbol{v})$, $H_y(\boldsymbol{r}, \boldsymbol{v})$ and $p_{\alpha\beta}(\boldsymbol{v})$ for a PCRPFV beam are given as follows [53]

$$H_\alpha(\boldsymbol{r}, \boldsymbol{v}) = \frac{\alpha}{w_0} \exp(-\frac{r^2}{w_0^2}) \exp(il\varphi) \exp(-ik\boldsymbol{r} \cdot \boldsymbol{v}), (\alpha = x, y), \tag{9}$$

$$p_{\alpha\beta}(\boldsymbol{v}) = \frac{k^2 B_{\alpha\beta} \sigma_{\alpha\beta}^2}{2\pi} \exp(-k^2 \sigma_{\alpha\beta}^2 v^2 / 2), \tag{10}$$

where $k = \pi/\lambda$ is the wavenumber. It follows from Eq. (10) that the elements $p_{xx}(\boldsymbol{v})$ and $p_{yy}(\boldsymbol{v})$ are non-negative functions because $\exp(-k^2 \sigma_{\alpha\beta}^2 v^2 / 2)$ is larger than zero for any value v. Thus, the first and the second inequalities in Eq. (8) are always true. Substituting Eq. (10) into the

third inequality in Eq. (8), we obtain

$$B_{xx}B_{yy}\sigma_{xx}^2\sigma_{yy}^2 \exp[-\frac{k^2\left(\sigma_{xx}^2+\sigma_{yy}^2\right)\nu^2}{2}] \geq \left|B_{xy}\right|^2 \sigma_{xy}^4 \exp(-k^2\sigma_{xy}^2\nu^2). \tag{11}$$

Equation (11) has to be met for any ν. Since the functions on the left-hand side and right-hand side of Eq. (11) decrease monotonically with ν, on considering the inequality for the limiting cases $\nu = 0$ and $\nu \to \infty$, the following ν-independent inequality is found:

$$\sqrt{\frac{\sigma_{xx}^2+\sigma_{yy}^2}{2}} \leq \sigma_{xy} \leq \sqrt{\frac{\sigma_{xx}\sigma_{yy}}{\left|B_{xy}\right|}}, \tag{12}$$

and therefore the modulus of B_{xy} has to fulfill the following condition:

$$\left|B_{xy}\right| \leq \frac{2\sigma_{xx}\sigma_{yy}}{\sigma_{xx}^2+\sigma_{yy}^2}. \tag{13}$$

For a PCRPFV beam generated by a Schell-model source, besides the restrictions on the parameters B_{xy}, σ_{xx}, σ_{yy} and σ_{xy} shown in Eq. (13), the following two additional conditions should be satisfied:

(A) Any point of the beam in the source plane is linearly polarized, which means that the minor semi-axes of the polarization ellipse equals to zero;

(B) The orientation angle of the polarization at any point in the source plane should satisfy $\theta(r) = \arctan(y/x)$.

According to [55], the major and minor semi-axes of the polarization ellipse, A_1 and A_2, as well as its degree of ellipticity ε and its orientation angle θ of the completely polarized part of a PCRPFV beam in the source plane are expressed as

$$A_{1,2}(r) = \frac{1}{\sqrt{2}}\left\{\sqrt{\left[W_{xx}(r,r)-W_{yy}(r,r)\right]^2+4\left|W_{xy}(r,r)\right|^2}\right.$$
$$\left.\pm\sqrt{\left[W_{xx}(r,r)-W_{yy}(r,r)\right]^2+4\left|\mathrm{Re}[W_{xy}(r,r)]\right|^2}\right\}^{1/2}, \tag{14}$$

$$\varepsilon(r) = A_2(r)/A_1(r), \tag{15}$$

$$\theta(\mathbf{r}) = \frac{1}{2}\arctan\left\{\frac{2\,\mathrm{Re}\left[W_{xy}(\mathbf{r},\mathbf{r})\right]}{W_{xx}(\mathbf{r},\mathbf{r})-W_{yy}(\mathbf{r},\mathbf{r})}\right\}. \tag{16}$$

Substituting Eq. (2) into Eqs. (14)–(16), we obtain the following expressions

$$\tan[2\theta(\mathbf{r})] = \mathrm{Re}\left[B_{xy}\right]\frac{2y/x}{1-(y/x)^2}. \tag{17}$$

The additional condition (A) requires that $A_1 = 0$, and applying Eqs. (2) and (14), one can obtain the following restriction on B_{xy}

$$\mathrm{Im}\left[B_{xy}\right] = 0. \tag{18}$$

With the requirements of the additional condition (B), and applying Eq. (17), one can obtain the following expression

$$\mathrm{Re}\left[B_{xy}\right] = 1. \tag{19}$$

It follows from Eqs. (18)–(19) that $B_{xy} = 1$. Under this condition and combining Eq. (13), one can easily obtain

$$\sigma_{xx} = \sigma_{yy} = \sigma_{xy} = \sigma_{yx}. \tag{20}$$

Finally, the realizability conditions of a PCRPFV beam can be expressed together as

$$B_{xx} = B_{yy} = B_{xy} = B_{yx} = 1, \sigma_{xx} = \sigma_{yy} = \sigma_{xy} = \sigma_{yx} = \sigma_g. \tag{21}$$

Then applying Eqs. (2) and (21), the CSD matrix of a PCRPFV beam in the source plane can be obtained as follows

$$W_{\alpha\beta}(\mathbf{r}_1, \mathbf{r}_2) = \frac{\alpha\beta}{w_0^2} \exp\left(-\frac{r_1^2 + r_2^2}{w_0^2}\right) \exp\left[-il(\varphi_1 - \varphi_2)\right] \exp\left[-\frac{(\mathbf{r}_1 - \mathbf{r}_2)^2}{2\sigma_g^2}\right], (\alpha, \beta = x, y). \tag{22}$$

3. Statistical properties of a PCRPFV beam on propagation

3.1. Propagation formulas of a PCRPFV beam

In this section, we will derive the propagation formulas for a PCRPFV beam passing through a stigmatic ABCD optical system and analyze the statistical properties of such a beam focused by a thin lens. It is to be noted that a beam can only possess a fractional TC in the generation plane, and this beam can be decomposed in terms of beams with integer TCs. On propagation, the light field must be continuous in space, and therefore has an integer topological charge [58]. Thus, the propagation of a PCRPFV beam can be regarded as the superimposed evolution of different partially coherent radially polarized integer vortex beams with different integer TCs. Here we use the convolution method to avoid complicated superposition calculations.

Within the validity of the paraxial approximation, propagation of the elements of the CSD matrix of a partially coherent vector beam through a stigmatic ABCD optical system can be studied with the help of the extended Collins formula [56]

$$W_{\alpha\beta}(\boldsymbol{\rho}_1, \boldsymbol{\rho}_2) = \frac{k^2}{4\pi^2 B^2} \int \int W_{\alpha\beta}(\mathbf{r}_1, \mathbf{r}_2) \exp\left(-\frac{ikA}{2B}r_1^2 + \frac{ik}{B}\mathbf{r}_1 \cdot \boldsymbol{\rho}_1 - \frac{ikD}{2B}\rho_1^2\right)$$
$$\times \exp\left(\frac{ikA}{2B}r_2^2 - \frac{ik}{B}\mathbf{r}_2 \cdot \boldsymbol{\rho}_2 + \frac{ikD}{2B}\rho_2^2\right) d^2\mathbf{r}_1 d^2\mathbf{r}_2, \tag{23}$$

where $\boldsymbol{\rho}_1$ and $\boldsymbol{\rho}_2$ are transverse position vectors in the output plane. A, B, C and D denote optical system transfer matrix elements.

Substituting Eq. (22) into Eq. (23), one obtains the following expressions for specific elements of the CSD matrix of a PCRPFV beam with the help of the convolution method [53],

$$W_{xx}(\boldsymbol{\rho}, \boldsymbol{\rho}) = I_x(\boldsymbol{\rho}) = \lambda^2 \frac{k^2}{4\pi^2 B^2} \int \int \left|\tilde{A}_x\left(\frac{\boldsymbol{v}}{\lambda} + \frac{\boldsymbol{\rho}}{\lambda B}\right)\right|^2 p\left(\frac{\boldsymbol{v}}{\lambda}\right) d^2\frac{\boldsymbol{v}}{\lambda}, \tag{24}$$

$$W_{yy}(\boldsymbol{\rho}, \boldsymbol{\rho}) = I_y(\boldsymbol{\rho}) = \lambda^2 \frac{k^2}{4\pi^2 B^2} \int \int \left|\tilde{A}_y\left(\frac{\boldsymbol{v}}{\lambda} + \frac{\boldsymbol{\rho}}{\lambda B}\right)\right|^2 p\left(\frac{\boldsymbol{v}}{\lambda}\right) d^2\frac{\boldsymbol{v}}{\lambda}, \tag{25}$$

$$W_{xy}(\boldsymbol{\rho}, \boldsymbol{\rho}) = \lambda^2 \frac{k^2}{4\pi^2 B^2} \int \int \tilde{A}_x^*\left(\frac{\boldsymbol{v}}{\lambda} + \frac{\boldsymbol{\rho}}{\lambda B}\right)\tilde{A}_y\left(\frac{\boldsymbol{v}}{\lambda} + \frac{\boldsymbol{\rho}}{\lambda B}\right) p\left(\frac{\boldsymbol{v}}{\lambda}\right) d^2\frac{\boldsymbol{v}}{\lambda}, \tag{26}$$

$$W_{yx}(\boldsymbol{\rho}, \boldsymbol{\rho}) = \lambda^2 \frac{k^2}{4\pi^2 B^2} \int \int \tilde{A}_y^*\left(\frac{\boldsymbol{v}}{\lambda} + \frac{\boldsymbol{\rho}}{\lambda B}\right)\tilde{A}_x\left(\frac{\boldsymbol{v}}{\lambda} + \frac{\boldsymbol{\rho}}{\lambda B}\right) p\left(\frac{\boldsymbol{v}}{\lambda}\right) d^2\frac{\boldsymbol{v}}{\lambda} \tag{27}$$

$$W_{xx}(0, \boldsymbol{\rho}) = \frac{1}{B^2} \exp\left[i\pi\lambda BD\left(\frac{\boldsymbol{\rho}}{\lambda B}\right)^2\right] \int \int \tilde{A}_x^*\left(\frac{\boldsymbol{v}}{\lambda}\right) p\left(\frac{\boldsymbol{v}}{\lambda}\right)\tilde{A}_x\left(\frac{\boldsymbol{v}}{\lambda} + \frac{\boldsymbol{\rho}}{\lambda B}\right) d^2\frac{\boldsymbol{v}}{\lambda}, \tag{28}$$

$$W_{yy}(0, \boldsymbol{\rho}) = \frac{1}{B^2} \exp\left[i\pi\lambda BD\left(\frac{\boldsymbol{\rho}}{\lambda B}\right)^2\right] \int\int \tilde{A}_y^*\left(\frac{\boldsymbol{v}}{\lambda}\right) p\left(\frac{\boldsymbol{v}}{\lambda}\right) \tilde{A}_y\left(\frac{\boldsymbol{v}}{\lambda} + \frac{\boldsymbol{\rho}}{\lambda B}\right) d^2\frac{\boldsymbol{v}}{\lambda}, \tag{29}$$

$$W_{xy}(0, \boldsymbol{\rho}) = \frac{1}{B^2} \exp\left[i\pi\lambda BD\left(\frac{\boldsymbol{\rho}}{\lambda B}\right)^2\right] \int\int \tilde{A}_x^*\left(\frac{\boldsymbol{v}}{\lambda}\right) p\left(\frac{\boldsymbol{v}}{\lambda}\right) \tilde{A}_y\left(\frac{\boldsymbol{v}}{\lambda} + \frac{\boldsymbol{\rho}}{\lambda B}\right) d^2\frac{\boldsymbol{v}}{\lambda}, \tag{30}$$

$$W_{yx}(0, \boldsymbol{\rho}) = \frac{1}{B^2} \exp\left[i\pi\lambda BD\left(\frac{\boldsymbol{\rho}}{\lambda B}\right)^2\right] \int\int \tilde{A}_y^*\left(\frac{\boldsymbol{v}}{\lambda}\right) p\left(\frac{\boldsymbol{v}}{\lambda}\right) \tilde{A}_x\left(\frac{\boldsymbol{v}}{\lambda} + \frac{\boldsymbol{\rho}}{\lambda B}\right) d^2\frac{\boldsymbol{v}}{\lambda}, \tag{31}$$

with

$$A_x(\boldsymbol{r}) = \frac{x}{w_0} \exp\left(-\frac{x^2 + y^2}{w_0^2}\right) \exp(il\varphi) \exp\left(ikAr^2/2B\right), \tag{32}$$

$$A_y(\boldsymbol{r}) = \frac{y}{w_0} \exp\left(-\frac{x^2 + y^2}{w_0^2}\right) \exp(il\varphi) \exp\left(ikAr^2/2B\right), \tag{33}$$

$$p(\boldsymbol{v}) = \frac{k^2\sigma_g^2}{2\pi} \exp\left(-k^2\sigma_g^2 v^2/2\right), \tag{34}$$

where $\tilde{A}_\gamma$ $(\gamma = x, y)$ denotes the Fourier-transform operation of $\tilde{A}_\gamma$.

The average intensity and the DOP at point $\boldsymbol{\rho}$ in the output plane are given as

$$I(\boldsymbol{\rho}) = W_{xx}(\boldsymbol{\rho}, \boldsymbol{\rho}) + W_{yy}(\boldsymbol{\rho}, \boldsymbol{\rho}), \tag{35}$$

$$P(\boldsymbol{\rho}) = \sqrt{1 - \frac{4\text{Det}\left[\overleftrightarrow{W}(\boldsymbol{\rho}, \boldsymbol{\rho})\right]}{\left\{\text{Tr}\left[\overleftrightarrow{W}(\boldsymbol{\rho}, \boldsymbol{\rho})\right]\right\}^2}}, \tag{36}$$

where Det and Tr denote the determinant and the trace of the matrix, respectively.

The CSD matrix of a PCRPFV beam can be represented as a sum of a polarized part and a unpolarized part [59]

$$\overleftrightarrow{W}(\boldsymbol{\rho}, \boldsymbol{\rho}) = \overleftrightarrow{W}^p(\boldsymbol{\rho}, \boldsymbol{\rho}) + \overleftrightarrow{W}^u(\boldsymbol{\rho}, \boldsymbol{\rho}), \tag{37}$$

$$\overleftrightarrow{W}^p(\boldsymbol{\rho}, \boldsymbol{\rho}) = \begin{pmatrix} B(\boldsymbol{\rho}, \boldsymbol{\rho}) & D(\boldsymbol{\rho}, \boldsymbol{\rho}) \\ D^*(\boldsymbol{\rho}, \boldsymbol{\rho}) & C(\boldsymbol{\rho}, \boldsymbol{\rho}) \end{pmatrix}, \tag{38}$$

$$\overleftrightarrow{W}^u(\boldsymbol{\rho}, \boldsymbol{\rho}) = \begin{pmatrix} A(\boldsymbol{\rho}, \boldsymbol{\rho}) & 0 \\ 0 & A(\boldsymbol{\rho}, \boldsymbol{\rho}) \end{pmatrix}, \tag{39}$$

with

$$A(\boldsymbol{\rho}, \boldsymbol{\rho}) = \frac{1}{2}\left[W_{xx}(\boldsymbol{\rho}, \boldsymbol{\rho}) + W_{yy}(\boldsymbol{\rho}, \boldsymbol{\rho}) - \sqrt{\left[W_{xx}(\boldsymbol{\rho}, \boldsymbol{\rho}) - W_{yy}(\boldsymbol{\rho}, \boldsymbol{\rho})\right]^2 + 4\left|W_{xy}(\boldsymbol{\rho}, \boldsymbol{\rho})\right|^2}\right], \tag{40}$$

$$B(\boldsymbol{\rho}, \boldsymbol{\rho}) = \frac{1}{2}\left[W_{xx}(\boldsymbol{\rho}, \boldsymbol{\rho}) - W_{yy}(\boldsymbol{\rho}, \boldsymbol{\rho}) + \sqrt{\left[W_{xx}(\boldsymbol{\rho}, \boldsymbol{\rho}) - W_{yy}(\boldsymbol{\rho}, \boldsymbol{\rho})\right]^2 + 4\left|W_{xy}(\boldsymbol{\rho}, \boldsymbol{\rho})\right|^2}\right], \tag{41}$$

$$C(\boldsymbol{\rho}, \boldsymbol{\rho}) = \frac{1}{2}\left[W_{yy}(\boldsymbol{\rho}, \boldsymbol{\rho}) - W_{xx}(\boldsymbol{\rho}, \boldsymbol{\rho}) + \sqrt{\left[W_{xx}(\boldsymbol{\rho}, \boldsymbol{\rho}) - W_{yy}(\boldsymbol{\rho}, \boldsymbol{\rho})\right]^2 + 4\left|W_{xy}(\boldsymbol{\rho}, \boldsymbol{\rho})\right|^2}\right], \tag{42}$$

$$D(\boldsymbol{\rho}, \boldsymbol{\rho}) = W_{xy}(\boldsymbol{\rho}, \boldsymbol{\rho}). \tag{43}$$

The spectral intensities of the polarized part $I^p(\boldsymbol{\rho})$ and unpolarized part $I^u(\boldsymbol{\rho})$ are expressed respectively as follows

$$I^p(\boldsymbol{\rho}) = W_{xx}^p(\boldsymbol{\rho}, \boldsymbol{\rho}) + W_{yy}^p(\boldsymbol{\rho}, \boldsymbol{\rho}), \tag{44}$$

$$I^u(\boldsymbol{\rho}) = W_{xx}^u(\boldsymbol{\rho}, \boldsymbol{\rho}) + W_{yy}^u(\boldsymbol{\rho}, \boldsymbol{\rho}). \tag{45}$$

The SOP of the polarized portion can be characterized by the polarization ellipse, whose major and minor semi-axes of the ellipse, $A_1(\boldsymbol{\rho})$ and $A_2(\boldsymbol{\rho})$, as well as its degree of ellipticity,

$\varepsilon\,(\boldsymbol{\rho})$, and its orientation angle, $\theta\,(\boldsymbol{\rho})$, can be related directly to the elements of the cross-spectral density matrix $\overleftrightarrow{W}\,(\boldsymbol{\rho}, \boldsymbol{\rho})$ by the relations given in Eqs. (13)–(15). Note that it is necessary to replace the source plane parameters in Eqs. (14)–(16) with the output plane parameters.

3.2. Intensity distribution of a PCRPFV beam

As an example, we will study the propagation of a PCRPFV beam which passes through a thin lens with focal length f and then arrives at an output plane. The distances from the source to the thin lens and from the thin lens to the output plane are f and z, respectively. The transfer matrix between the source plane and the output plane reads as

$$\begin{pmatrix} A & B \\ C & D \end{pmatrix} = \begin{pmatrix} 1 & z \\ 0 & 1 \end{pmatrix}\begin{pmatrix} 1 & 0 \\ -1/f & 1 \end{pmatrix} = \begin{pmatrix} 1 - z/f & z \\ -1/f & 1 \end{pmatrix}. \tag{46}$$

Applying Eqs. (24)–(25) and (35), we calculate in Figs. 1 and 2 the average intensity distribution I and its components I_x and I_y of a focused PCRPFV beam by a thin lens at several propagation distances z for different values of the coherence width σ_g. The parameters used in the calculation are taken to be $\lambda = 632.8$nm, $w_0 = 1$mm, $l = 1.5$ and $f = 400$mm. We infer from Figs. 1–2 that a PCRPFV beam is distinguished from a partially coherent radially polarized integer vortex beam and a partially coherent radially polarized beam [40] in terms of the intensity pattern, which initially ($z = 0.1f$) possesses a radial opening in the annular ring encompassing the dark core. This opening arises due to the discontinuity of the phase in the source plane. It is to be noted that the intensity of the proposed PCRPFV beam in the source plane is independent of TC, according to Eq. (22), and the vortex phase is only exhibited in the intensity after propagation. The opening gap rotates clockwise as z increases (or rotates anticlockwise for negative l, which is not shown here), and up to 90 degrees at the focal plane ($z = f$). This rotation characteristic therefore originates from the handedness of the beam's azimuthal phase twist, which combines with the propagation phase. With a decrease of the coherence width, the opening gap profile at the focal plane disappears gradually and it finally becomes a Gaussian profile [Fig. 2(e1)], which is same behavior as that of a scalar partially coherent fractional vortex beam [53]. In addition, due the introduction of fractional vortex phase, the intensity distributions of the components I_x and I_y are different, i.e., the beam spot of the I_x of a focused PCRPFV beam possesses an opening
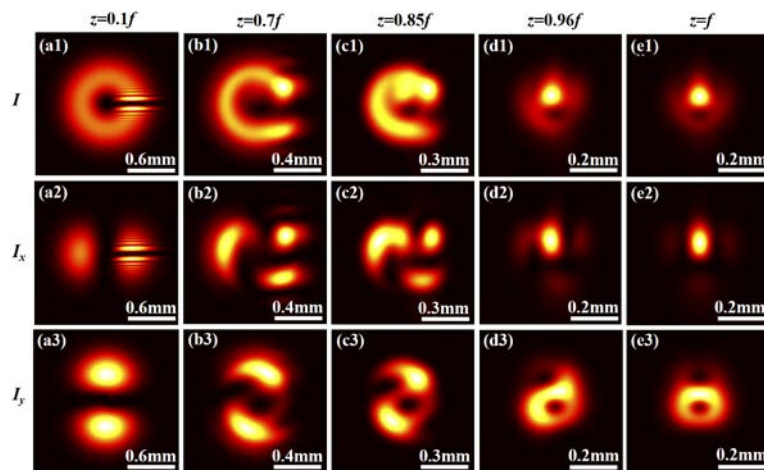

Fig. 1. Average intensity distribution I and its component I_x and I_y of a focused PCRPFV beam with $l = 1.5$ in the $x - y$ plane at several propagation distances z with $\sigma_g = 3$mm.

gap profile similar to the average intensity I, while the beam spot of the I_y does not exhibit such a property. This phenomenon of coherence-induced as well as vortex phase-induced beam shaping and the vortex phase-induced rotation of the beam spot can be used for manipulating particles which can only be trapped with special intensity distributions.
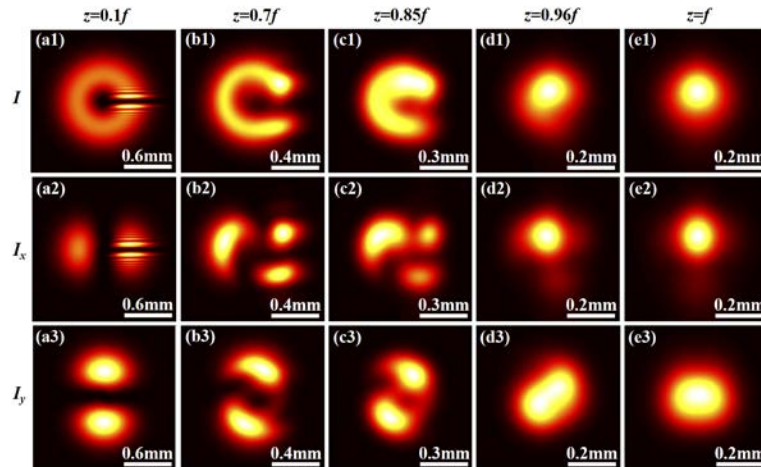

Fig. 2. Average intensity distribution I and its component I_x and I_y of a focused PCRPFV beam with $l = 1.5$ in the $x − y$ plane at several propagation distances z with $\sigma_g = 0.8$mm.

3.3. Degree of polarization of a PCRPFV beam

Now we analyze the polarization properties of a focused PCRPFV beam on propagation. We calculate in Fig. 3 the DOP (cross line $y = 0$) of partially coherent radially polarized vortex beams with different TCs in the focal plane. One finds from Fig. 3 that DOP of a PCRPFV beam is much different from that of a partially coherent radially polarized integer vortex beam. For a partially coherent radially polarized integer vortex beam ($l = 1$ and $l = 2$), the DOP near the point $(0,0)$ increases as the value of TC increases [40], while for a PCRPFV beam ($l = 1.2$, $l = 1.5$ and $l = 1.7$), the DOP first decreases and then increase as TC increases.
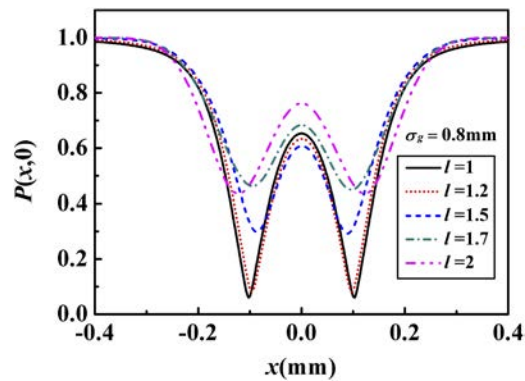
Fig. 3. Degree of polarization of a focused partially coherent radially polarized vortex beam (cross line $y = 0$) in the focal plane for different values of the topological charge l with $\sigma_g = 0.8$mm.

In Fig. 4 we calculate the cross lines of the normalized intensity distribution $I^p(x,0)/\max[I(x,0)]$ (solid black line), $I^u(x,0)/\max[I(x,0)]$ (short dashed red line), $I(x,0)/\max[I(x,0)]$ (long dashed blue line) of the focused PCRP vortex beam at several propagation distances for different values of topological charge l with $f = 400$mm, $\lambda = 632.8$nm, and $\sigma_g = 0.2$mm. Here I^p, I^u and I represent the intensity distribution of the polarized part, the intensity distribution of the unpolarized part and the total intensity distribution, respectively. From Fig. 4 we know that the total intensity distribution is determined by the polarized part and the unpolarized part together. When the propagation distance is short ($z = 150$mm), the contribution of the polarized parts plays a dominant role, thus the total intensity distribution is close to the polarized part [see Figs. 4(a) and 4(d)]. With the incease of the propagation distance, the contribution of the unpolarized part gradually increases. For the case of $l = 1$, when $z = 290$mm, the contribution of the unpolarized part is the same as the that of the polarized part, thus the total intensity distribution exhibits a flat-topped beam profile [see Fig. 4(b)]. When the propagation distance is long enough ($z = 400$mm), the contribution of the unpolarized parts plays a dominant role, thus the total intensity distribution is close to the unpolarized part [see Fig. 4(c)]. In addition, we found that due to the introduction of fractional topological charge, the symmetry of intensity distribution in the transmission process was broken [see Figs. 4(d) and 4(e)], but the symmetry was restored at the focal plane [see Fig. 4(f)].
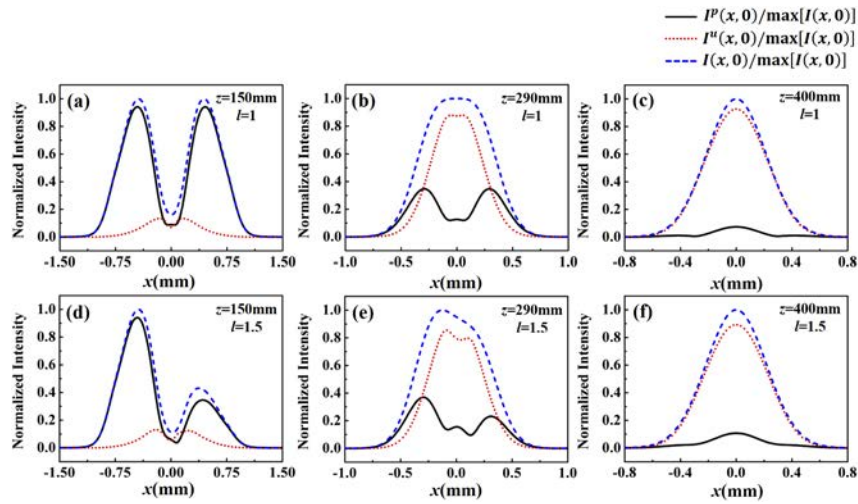

Fig. 4. Cross lines of the normalized intensity distributions $I^p(x,0)/\max[I(x,0)]$ (solid black line), $I^u(x,0)/\max[I(x,0)]$ (short dashed red line), $I(x,0)/\max[I(x,0)]$ (long dashed blue line) of a focused partially coherent radially polarized vortex beam at several propagation distances for different values of topological charge l.

To understand better about the transition of power from the polarized part to the unpolarized part on propagation, we now study the evolution properties of the integrated normalized intensities of the polarized part and unpolarized part, which are defined as [21]

$$\eta^m = \frac{\int I^m(\boldsymbol{\rho})\,\mathrm{d}^2\boldsymbol{\rho}}{\int I(\boldsymbol{\rho})\,\mathrm{d}^2\boldsymbol{\rho}}, (m = p, u), \tag{47}$$

where η^p and η^u denote the integrated normalized intensities of the polarized part and the unpolarized part, respectively.

We calculate in Figs. 5 (a) and 5(b) the variation of η^p and η^u of a focused partially coherent radially polarized vortex beam with different values of the topological charge l versus the
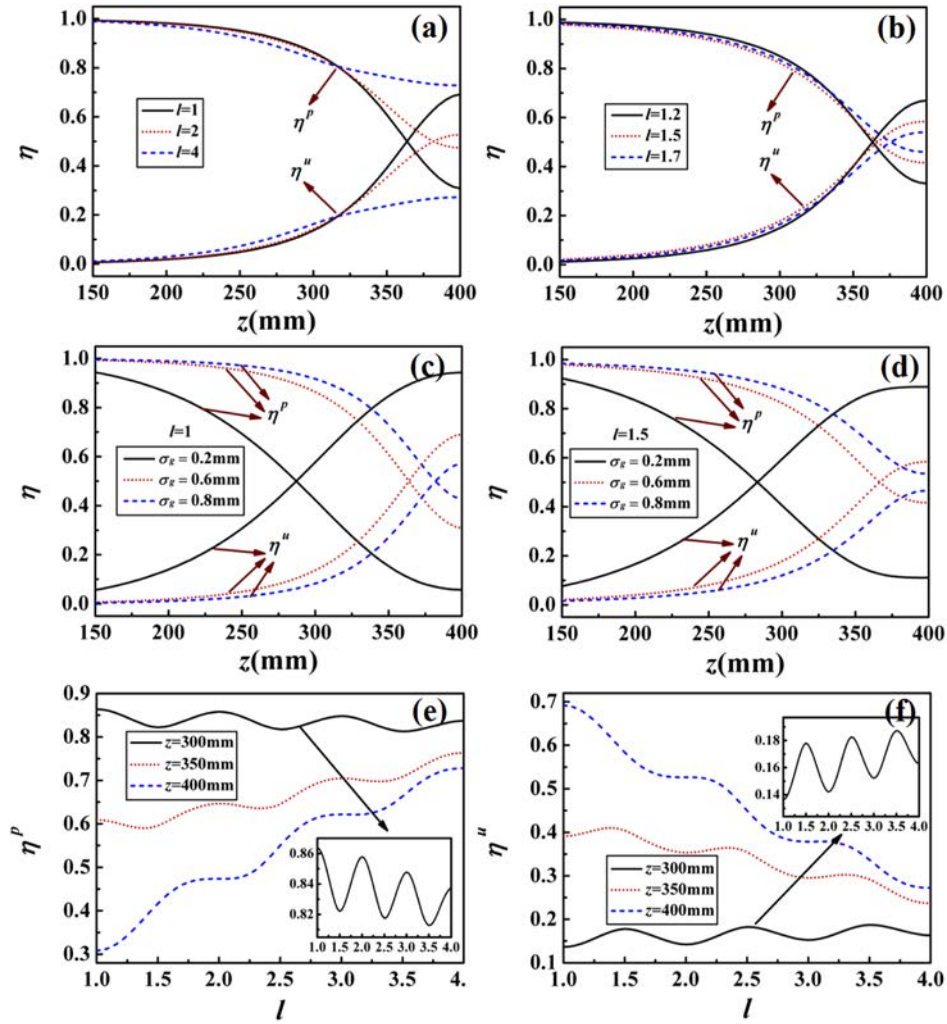
Fig. 5. Variation of the integrated normalized intensities of the polarized part (η^p) and the unpolarized part (η^u) of a focused partially coherent radially polarized vortex beam for (a-b) different values of the topological charge l with $\sigma_g = 0.6$mm versus the propagation distance z, (c-d) different values of the initial coherence width σ_g versus the propagation distance z and (e-f) different propagation distance z versus the topological charge l.

propagation distance l with $\sigma_g = 0.6$mm. From Figs. 5 (a) and 5(b), we find that regardless of whether the topological charge is an integer or a fraction, η^p decreases on propagation, while the η^u increases, which means that the beam becomes depolarized (i.e., the power transits from the polarized part to the unpolarized part on propagation). This is also supported by the results in Fig. 4 and the behavior is quite different from that of a coherent beam.

Figures 5(a) and 5(b) also show, however, that this depolarization can be mitigated by increasing the topological charge. This is because that the vortex phase improves resistance to the coherence-induced degradation of the intensity distribution and results in the anti-depolarization effect. The distance as which $\eta^p = \eta^u$ is the position at which the unpolarized part of the field becomes stronger than the polarized part. This distance increases with l, and for sufficiently large topological charge (in this case $l = 4$), this crossing never occurs and the polarized part of the

field always remains dominant. Evidently, the vortex phase plays an anti-depolarization role for this class of beams. Figures 5(c) and 5(d) show, in contrast, that a decrease in coherence reduces the distance at which $\eta^p = \eta^u$; partial coherence has a depolarizing effect.

Figures 5(e) and (f) show how the integrated normalized intensities vary with topological charge for several propagation distances, for a fixed coherence width $\sigma_g = 0.6$mm. Although η^p increases monotonously with TC (regardless of an integer or a fraction) at near-focal plane ($z = 400$mm), but it is worth noting the different effects of the integer vortex phase and the fractional vortex phase at far-focal plane ($z = 300$mm). With the increment of l, η^p (or η^u) of a partially coherent radially polarized integer vortex beam (e.g., $l = 1, 2, 3, 4$) is monotonically decreasing (or increasing)(see insets), which means that the integer vortex phase plays a role of anti-depolarization, while for a PCRPFV beam (i.e., l is fractional), η^p first decreases (e.g., from 1.1 to 1.5) and then increases (e.g, from 1.5-1.9) between two integers, which means that the fractional vortex phase first plays a role of depolarization and then plays a role anti-depolarization between two integers.

3.4. State of polarization of a PCRPFV beam

We calculate in Fig. 6 the variation of the state of polarization of a focused partially coherent radially polarized vortex beam with different values of the topological charge l at several propagation distances for $\sigma_g = 0.8$mm. One finds from Figs. 6(a1)-(a4) that the SOP of a focused partially coherent radially polarized beam with no-vortex phase ($l = 0$) remains invariant on propagation and always displays radial polarization as expected [20]. While by introducing the vortex phase into the partially coherent radially polarized beam (i.e., a partially coherent radially polarized vortex beam) [Figs. 6(b1)-(c4)], we find that the radial polarization disappears and elliptical polarization appears on propagation. The SOP displays right-handed elliptical
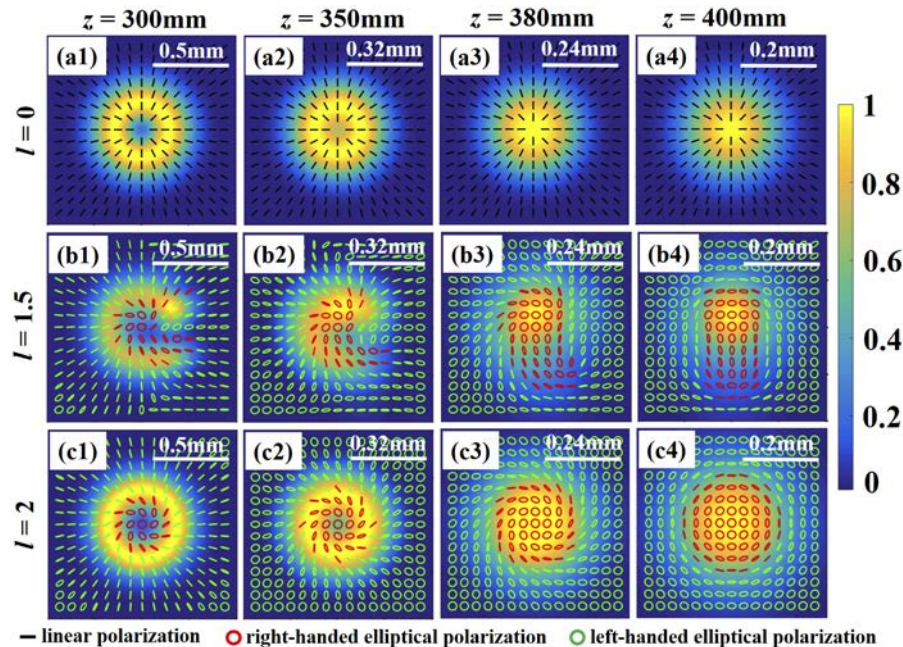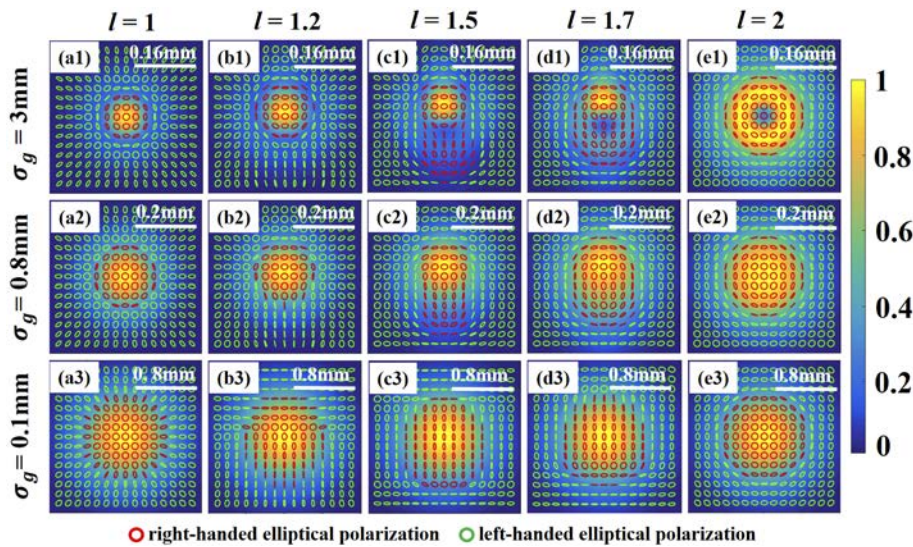

Fig. 6. Variation of the state of polarization of a focused partially coherent radially polarized vortex beam with different values of the topological charge l at several propagation distances for $\sigma_g = 0.8$mm.

polarization around the beam center and left-handed elliptical polarization outside of the beam center with positive TC (the handedness of the polarization ellipse is reversed for negative TC, which is not shown here). Furthermore, in contrast with the SOP distribution of a partially coherent radially polarized integer vortex beam ($l = 2$), that of a PCRPFV beam ($l = 1.5$) is less symmetric due to its asymmetric intensity distribution, especially at the non-focal plane [Figs. 6(b1)-(b3)]. With the increase of z, the SOP distribution of a PCRPFV beam evolves from the messy distribution to bilateral symmetry [Figs. 6(b1)-(b4)].

To learn more about the influence of TC and coherence width on the SOP, we calculate in Fig. 7 the variation of the SOP of a focused partially coherent radially polarized vortex beam with different values of the TC l at focal plane for different values of σ_g. One finds that as l varies, the SOP varies, and the closer the value of the TC is to an integer, the more symmetric the SOP distribution is. Moreover, with the decrease of σ_g, the SOP distribution of a PCRPFV beam becomes more symmetric.

Fig. 7. Variation of the state of polarization of a focused partially coherent radially polarized vortex beam with different values of the topological charge l at focal plane for different values of σ_g.

3.5. Cross-spectral density matrix of a PCRPFV beam

In spite of their complex structure, it is possible to experimentally characterize some aspects of PCRPFV beam with relatively simple measurements. Fig. 8 shows the density plot of the modulus of the trace of the CSD matrix $|\text{Tr}[W(0, \boldsymbol{\rho})]|$ of PCRPFV beams in the focal plane with both different l values and different values of σ_g. The quantity $|\text{Tr}[W(0, \boldsymbol{\rho})]|$ is calculated from two matrix elements of the polarization matrix, which is used for describing the coherence and the polarization phenomena of a vector beam [60] and can be measured by the fourth-order correlation function method introduced in [61]. Regardless of the choice of coherence width, one finds that beams with different values of l have distinct patterns of $|\text{Tr}[W(0, \boldsymbol{\rho})]|$. It is to be noted that this pattern is not present in the intensity distribution of the beam, as all beams reduce to a Gaussian intensity profile in the low coherence limit. Fig. 8 suggests that it is possible to measure the TC of our PCRPFV beams by measuring $|\text{Tr}[W(0, \boldsymbol{\rho})]|$ due to the fact that the distribution of $|\text{Tr}[W(0, \boldsymbol{\rho})]|$ varies depending on TC. In particular, the distribution of
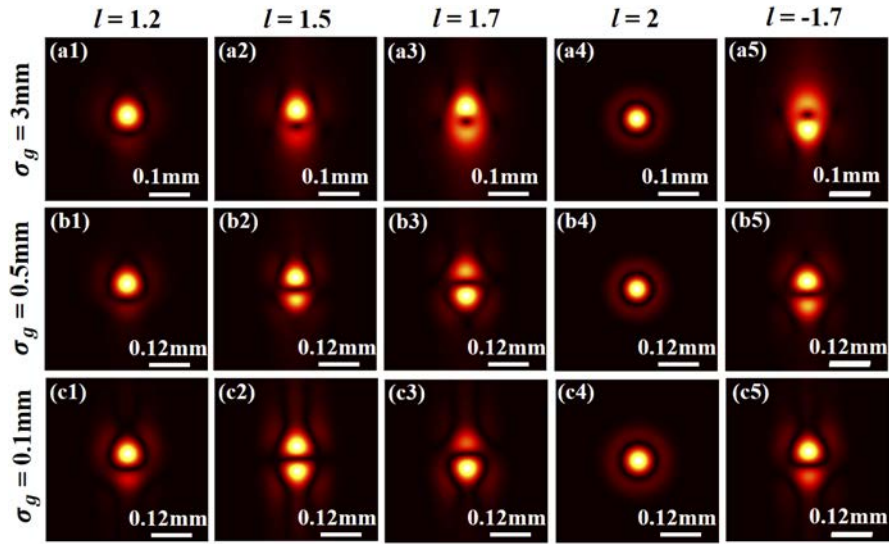
Fig. 8. Density plot of the modulus of the trace of the CSD matrix $|\text{Tr}\,[W\,(0, \boldsymbol{\rho})]|$ of a partially coherent radially polarized vortex beam with different l (both integral and fractional) focused by a lens at focal plane for different values of σ_g.

$|\text{Tr}\,[W\,(0, \boldsymbol{\rho})]|$ of a PCRPFV beam with $l = 1.5$ evolves from bilateral symmetry to rectangular symmetry on decreasing σ_g.

To further study the vector characteristics of a PCRPFV beam (namely, possessing directional components) and to learn more about the influence of coherence width on the CSD distribution of a PCRPFV beam, we calculate in Fig. 9 the density plot of the modulus of the trace of the CSD matrix $|\text{Tr}\,[W\,(0, \boldsymbol{\rho})]|$, together with the modulus of the elements of the CSD matrix $|W_{xx}\,(0, \boldsymbol{\rho})|$, $\left|W_{yy}\,(0, \boldsymbol{\rho})\right|$ and $\left|W_{xy}\,(0, \boldsymbol{\rho})\right|$ of a partially coherent radially polarized vortex beam with different l ($l = 2$ and $l = 1.5$) focused by a lens at focal plane for different values of σ_g. In contrast with a partially coherent radially polarized vortex beam with integer TC, whose pattern of $|\text{Tr}\,[W\,(0, \boldsymbol{\rho})]|$ is independent of the coherence width, the pattern of $|\text{Tr}\,[W\,(0, \boldsymbol{\rho})]|$ of a PCRPFV beam ($l = 1.5$) will split and become more symmetric by decreasing σ_g. In addition, regardless of the integer TC or fractional TC, the distributions of $|W_{xx}\,(0, \boldsymbol{\rho})|$, $\left|W_{yy}\,(0, \boldsymbol{\rho})\right|$ and $\left|W_{xy}\,(0, \boldsymbol{\rho})\right|$ can be split by decreasing σ_g. It is to be noted that patterns of $|W_{xx}\,(0, \boldsymbol{\rho})|$, $\left|W_{yy}\,(0, \boldsymbol{\rho})\right|$ and $\left|W_{xy}\,(0, \boldsymbol{\rho})\right|$ of a partially coherent radially polarized vortex beam with integer TC are always of rectangular symmetry regardless of the coherence width, while the symmetry of those of a PCRPFV beam ($l = 1.5$) will change and evolves from bilateral symmetry to rectangular symmetry with decreasing σ_g.
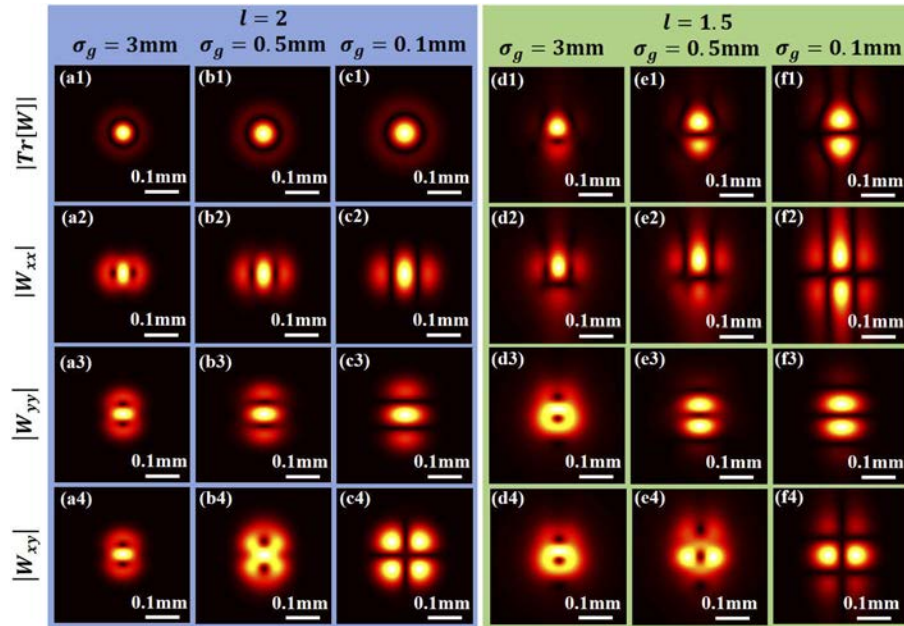
Fig. 9. Density plot of the modulus of the trace of the CSD matrix $|\text{Tr}\,[W\,(0,\boldsymbol{\rho})]|$, toghther with the modulus of the elements of the CSD matrix $|W_{xx}\,(0,\boldsymbol{\rho})|$, $\left|W_{yy}\,(0,\boldsymbol{\rho})\right|$ and $\left|W_{xy}\,(0,\boldsymbol{\rho})\right|$ of a partially coherent radially polarized vortex beam with different l ($l = 2$ and $l = 1.5$) focused by a lens at focal plane for different values of σ_g.

4. Experimental generation of a PCRPFV beam

In this section, we report the experimental generation of a PCRPFV beam. From Eqs. (2) and (3), it can be seen that the core challenges in generating PCRPFV beams lie in the introduction of partial coherence and the loading of a fractional vortex phase. In physical terms, a fractional vortex phase can be considered as a special phase containing a mixed screw-edge dislocation, in analogy with a crystal defect. In this paper, we employ a spiral phase plate (SPP) to load the fractional vortex phase, which was created in 1992 [62]. The SPP is a transparent plate with a polymer replicated on a glass substrate (Type: RPC Photonics u6243E), and its thickness varies azimuthally. Generally a SPP is designed especially for a specific wavelength λ_0 to load a vortex phase with a fixed integer TC l_0, and the phase delay imprinted by the SPP can be written as $(n - 1)\,h/\lambda_0 \cdot \text{mod}\,(l_0\psi, 2\pi)$, where "mod" represents modulus after division, n is the index of refraction of material, h is the thickness of SPP and $l_0 = (n - 1)h/\lambda_0$ is the generated integer TC in product design. Thus we can exploit dispersion to produce a fractional vortex phase with a laser source of wavelength λ but using a SPP with integer TC l_0 designed for another wavelength λ_0, and the generated fractional TC for laser source λ is $l = l_0\lambda_0/\lambda$.

Figure 10 shows our experimental setup for generating a PCRPFV beam and measuring its focused intensity. A laser beam emitted from a He-Ne laser ($\lambda = 632.8$nm) first passes through a linear polarizer (LP) and a beam expander (BE), then is reflected by a reflecting mirror (RM). The reflected beam focused by a thin lens L_1 ($f_1 = 150$mm) illuminates a rotating ground-glass disk (RGGD), generating an incoherent beam. Based on the Van Cittert-Zernike theorem [63], by passing through a collimation lens L_2 ($f_2 = 250$mm) and a Gaussian amplitude filter (GAF), the generated beam becomes a partially coherent with Gaussian statistics.

The generated partially coherent Gaussian beam goes towards the SPP. Here, we employ our laser source $\lambda = 632.8$nm instead to illuminate the SPP ($l = 1$) designed for the wavelength
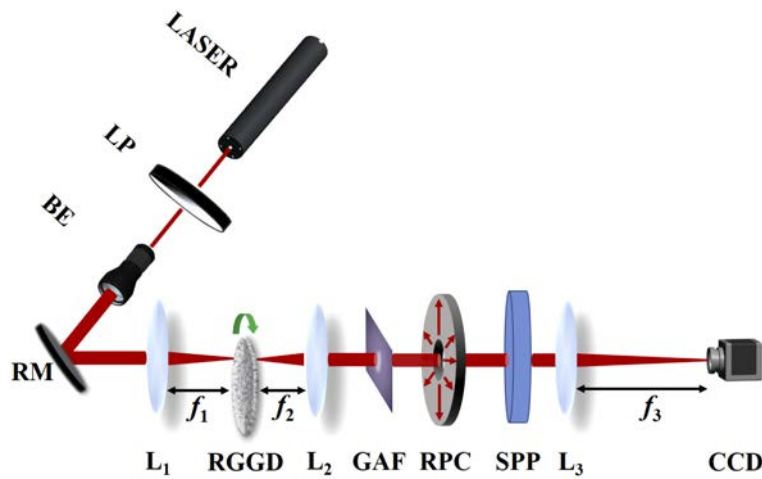
Fig. 10. Experimental setup for generating a PCRPFV beam and measuring its focused intensity. LASER, He-Ne laser; LP, linear polarizer; BE, beam expander; RM, reflecting mirror; L_1, L_2, L_3, thin lenses; RGGD, rotating ground-glass disk; GAF, Gaussian amplitude filter; RPC, radial polarization converter; SPP, spiral phase plate; CCD, charge-coupled device.

λ_0 = 959.8nm to generate screw-edge dislocations with fractional TC l = 1.5, the detail generation principle of fractional TC can be found in [64]. It is to be noted that, although Spatial Light Modulation is more flexible than SPP in generating and tuning beams with TC, SLMs have a complex response to polarization and possible technical collimation problems; we chose a SPP to load the vortex phase here. The coherence width of the generated PCRPFV beam is controlled by the focused beam spot on the RGGD and the roughness of the RGGD together. In our experiment, the roughness of the RGGD is fixed, so we mainly modulate the coherence width by varying the focused beam spot size on the RGGD. We have chosen two different beam spots on the RGGD to generate the PCRPFV beam with two different spatial coherence widths (σ_g = 3mm amd σ_g = 0.8mm). The detailed measurement method of coherence width can be found in [65]. The generated PCRPFV beam passes through a thin lens L_3 (f_3 = 400mm) , and then arrives at a charge coupled device (CCD). The CCD is used to measure not only the intensity distribution but also DOP with the help of a polarizer as well as quarter-wave plate [60].

Figures 11–12 show our experimental results of the average intensity distribution I and its component I_x and I_y of a focused PCRPFV beam with l = 1.5, at several propagation distances z with w_0 = 1mm, σ_g = 3mm and σ_g = 0.8mm, respectively. To measure I_x and I_y, we just put a linear polarizer whose transmission axis forms an angle φ = 0 or φ = 90° with x-axis. From Figs. 11–12, one finds that our experimental results clearly demonstrate the existence of the opening gap in average intensity as well as in its component I_x and the clockwise rotation (l = 1.5) of the opening gap, and the rotation angle of the opening gap becomes 90 degrees at the focal plane. In addition, decreasing the coherence width makes the intensity become a Gaussian profile, which agrees well with the numerical results in Figs. 1–2. Figure 13 shows our experimental results (red dotted curves) of the DOP of a focused PCRPFV beam with w_0 = 1mm and σ_g = 0.8mm versus the coordinate x in the focal plane. The black solid curve in Fig. 13 denotes the theoretical results. The detailed principle and process for measuring the DOP can be found in [60]. One finds from Fig. 13 that our experiment result agrees well with the theoretical result, and only a slight difference between experimental results and numerical results exists, which may be caused by the fluctuation of the source beam, non-ideal optical elements, and the resolution limits of the RPC and CCD.
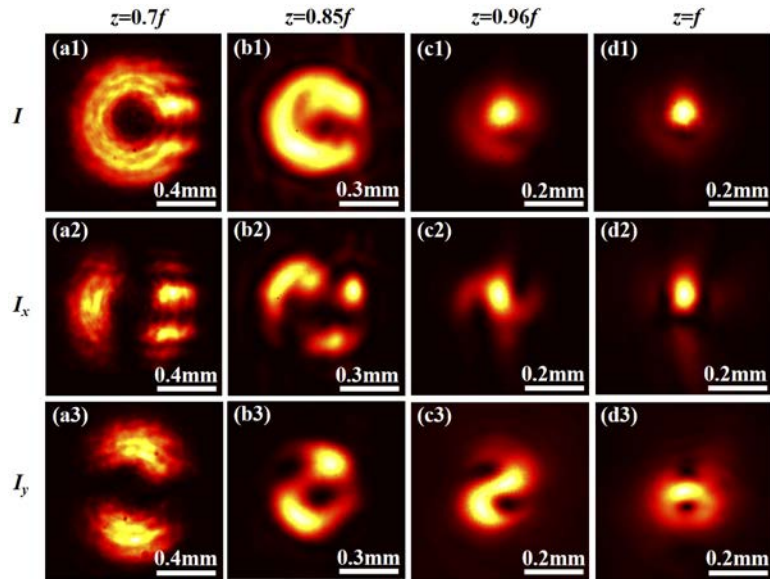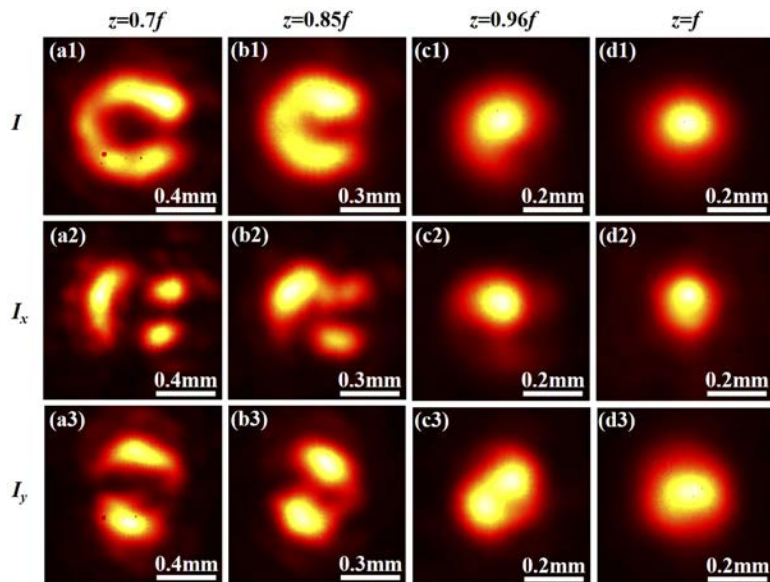
Fig. 11. Experimental results of the average intensity distribution I and its component I_x and I_y of a focused PCRPFV beam with $l = 1.5$, $w_0 = 1$mm and $\sigma_g = 3$mm in the $x - y$ plane at several propagation distances z.
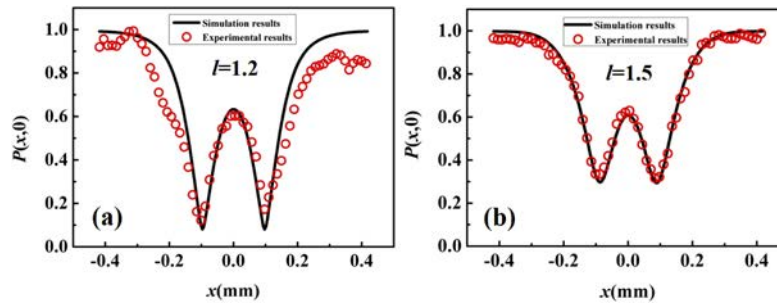

Fig. 12. Experimental results of the average intensity distribution I and its component I_x and I_y of a focused PCRPFV beam with $l = 1.5$, $w_0 = 1$mm and $\sigma_g = 0.8$mm in the $x - y$ plane at several propagation distances z.

Fig. 13. Experimental results (red dotted curve) of the degree of polarization of a focused PCRPFV beam with $w_0 = 1$mm and $\sigma_g = 0.8$mm versus the coordinate x in the focal plane.

5. Summary

We have introduced a new kind of partially coherent vector beam with radial polarization, as well as a fractional vortex phase, named partially coherent radially polarized fractional vortex beam, and discussed its realizability and beam conditions. Propagation formulae for the elements of the CSD matrix of a PCRPFV beam propagating through a stigmatic ABCD optical system have been derived, and the statistical properties of a PCRPFV beam focused by a thin lens have been studied numerically and compared with that of a partially coherent radially polarized integer vortex beam. We found that the topological charge and coherence width strogly determine the statistical properties of a PCRPFV beam. By introducing a fractional topological charge, the PCRPFV beam exhibits an intensity distribution that possesses a radial opening in the annular intensity ring encompassing the dark core, and the opening gap rotates gradually up to 90 degrees as the propagation distance increases.

The topological charge embedded in a PCRPFV beam brings different polarization characteristics at different propagation distances, e.g., at near-focal plane, the vortex phase plays a role of anti-depolarization, while at far-focal plane, with an increase of the topological charge, the vortex phase first plays a role of depolarization, and then plays a role of anti-depolarization. Furthermore, the PCRPFV beam exhibits a more symmetric SOP distribution and $|\text{Tr}\,[W\,(0,\boldsymbol{\rho})]|$ distribution depending on the magnitude of coherence width; in addition, decreasing the coherence width can make the distribution of $|W_{xx}\,(0,\boldsymbol{\rho})|$, $|W_{yy}\,(0,\boldsymbol{\rho})|$ and $|W_{xy}\,(0,\boldsymbol{\rho})|$ split. We have carried out experimental generation of a PCRPFV beam and verified our theoretical predictions.

The combined modulation of fractional vortex phase, polarization direction and coherence width enriches the structure of the intensity distribution of a PCRPFV beam. The Gaussian profile spot and profile spot with dark nucleus can be used for trapping particles with high refractive indices and low refractive indices, respectively. Thus, a PCRPFV beam can be used to trap particles with different refractive indices simply by suitably varying the spatial coherence width in one optical trap system. This provides significantly more flexibility than a coherent beams.

In addition, guiding particles and optical sorting can be realized by using intensity profile with fixed gap and self-rotating characteristic.

Furthermore, it was revealed that the vortex phase will induce changes of the state of polarization and the CSD distribution, and this phenomenon may be useful for detection of phase objects. Last but not least, the polarization lidar system is an effective tool to study the morphology of the shape of sand aerosol and other atmospheric non-spherical particles by measuring the depolarization ratio of backscattering light of non-spherical particles. In this paper, it is found that fractional-order vortex phase can induce different polarization characteristics at different propagation distances, so it has potential applications in polarization lidar systems.

Funding

Disclosures

The authors declare no conflicts of interest.

References

1. Q. Zhan, "Cylindrical vector beams: from mathematical concepts to applications," Adv. Opt. Photonics **1**(1), 1–57 (2009).
2. Y. Zhang, B. Ding, and T. Suyama, "Trapping two types of particles using a double-ring-shaped radially polarized beam," Phys. Rev. A **81**(2), 023831 (2010).
3. K. S. Youngworth and T. G. Brown, "Focusing of high numerical aperture cylindrical-vector beams," Opt. Express **7**(2), 77–87 (2000).
4. P. Wróbel, J. Pniewski, T. J. Antosiewicz, and T. Szoplik, "Focusing Radially Polarized Light by a Concentrically Corrugated Silver Film without a Hole," Phys. Rev. Lett. **102**(18), 183902 (2009).
5. E. Wolf, "Unified theory of coherence and polarization of random electromagnetic beams," Phys. Lett. A **312**(5-6), 263–267 (2003).
6. J. Tervo, T. Setälä, and A. T. Friberg, "Degree of coherence for electromagnetic fields," Opt. Express **11**(10), 1137–1143 (2003).
7. Y. Dong, F. Wang, C. Zhao, and Y. Cai, "Effect of spatial coherence on propagation, tight focusing, and radiation forces of an azimuthally polarized beam," Phys. Rev. A **86**(1), 013840 (2012).
8. T. Shirai, H. Kellock, T. Setälä, and A. T. Friberg, "Visibility in ghost imaging with classical partially polarized electromagnetic beams," Opt. Lett. **36**(15), 2880–2882 (2011).
9. X. Liu, F. Wang, M. Zhang, and Y. Cai, "Experimental demonstration of ghost imaging with an electromagnetic Gaussian Schell-model beam," J. Opt. Soc. Am. A **32**(5), 910–920 (2015).
10. O. Korotkova, "Scintillation index of a stochastic electromagnetic beam propagating in random media," Opt. Commun. **281**(9), 2342–2348 (2008).
11. A. T. Friberg and T. D. Visser, "Scintillation of electromagnetic beams generated by quasi-homogeneous sources," Opt. Commun. **335**, 82–85 (2015).
12. O. Korotkova, M. Salem, and E. Wolf, "Beam conditions for radiation generated by an electromagnetic Gaussian Schell-model source," Opt. Lett. **29**(11), 1173–1175 (2004).
13. O. Korotkova and E. Wolf, "Generalized Stokes parameters of random electromagnetic beams," Opt. Lett. **30**(2), 198–200 (2005).
14. T. Shirai and E. Wolf, "Correlations between intensity fluctuations in stochastic electromagnetic beams of any state of coherence and polarization," Opt. Commun. **272**(2), 289–292 (2007).
15. F. Gori, M. Santarsiero, R. Borghi, and V. Ramírez-Sánchez, "Realizability condition for electromagnetic Schell-model sources," J. Opt. Soc. Am. A **25**(5), 1016–1021 (2008).
16. B. Kanseri, S. Rath, and H. C. Kandpal, "Determination of the Beam Coherence-Polarization Matrix of a Random Electromagnetic Beam," IEEE J. Quantum Electron. **45**(9), 1163–1167 (2009).
17. M. Yao, Y. Cai, H. T. Eyyuboğlu, Y. Baykal, and O. Korotkova, "Evolution of the degree of polarization of an electromagnetic Gaussian Schell-model beam in a Gaussian cavity," Opt. Lett. **33**(19), 2266–2268 (2008).
18. Y. Dong, F. Feng, Y. Chen, C. Zhao, and Y. Cai, "Statistical properties of a nonparaxial cylindrical vector partially coherent field in free space," Opt. Express **20**(14), 15908–15927 (2012).
19. Y. Dong, Y. Cai, C. Zhao, and M. Yao, "Statistics properties of a cylindrical vector partially coherent beam," Opt. Express **19**(7), 5979–5992 (2011).
20. G. Wu, F. Wang, and Y. Cai, "Coherence and polarization properties of a radially polarized beam with variable spatial coherence," Opt. Express **20**(27), 28301–28318 (2012).
21. Y. Chen, F. Wang, L. Liu, C. Zhao, Y. Cai, and O. Korotkova, "Generation and propagation of a partially coherent vector beam with special correlation functions," Phys. Rev. A **89**(1), 013801 (2014).
22. F. Wang, Y. Cai, Y. Dong, and O. J. A. P. L. Korotkova, "Experimental generation of a radially polarized beam with controllable spatial coherence," Appl. Phys. Lett. **100**(5), 051108 (2012).
23. F. Wang, X. Liu, L. Liu, Y. Yuan, and Y. J. A. P. L. Cai, "Experimental study of the scintillation index of a radially polarized beam with controllable spatial coherence," Appl. Phys. Lett. **103**(9), 091102 (2013).
24. D. G. Grier, "A revolution in optical manipulation," Nature **424**(6950), 810–816 (2003).

25. J. Wang, J. Y. Yang, I. M. Fazal, N. Ahmed, Y. Yan, H. Huang, Y. Ren, Y. Yue, S. Dolinar, M. Tur, and A. E. Willner, "Terabit free-space data transmission employing orbital angular momentum multiplexing," Nat. Photonics **6**(7), 488–496 (2012).

26. J. Zeng, X. Liu, C. Zhao, F. Wang, G. Gbur, and Y. Cai, "Spiral spectrum of a Laguerre-Gaussian beam propagating in anisotropic non-Kolmogorov turbulent atmosphere along horizontal path," Opt. Express **27**(18), 25342–25356 (2019).

27. H. Zhang, J. Li, M. Guo, M. Duan, Z. Feng, and W. Yang, "Optical trapping two types of particles using a focused vortex beam," Optik **166**, 138–146 (2018).

28. X. Wang, G. Rui, L. Gong, B. Gu, and Y. Cui, "Manipulation of resonant metallic nanoparticle using 4Pi focusing system," Opt. Express **24**(21), 24143–24152 (2016).

29. F. Tamburini, G. Anzolin, G. Umbriaco, A. Bianchini, and C. Barbieri, "Overcoming the Rayleigh Criterion Limit with Optical Vortices," Phys. Rev. Lett. **97**(16), 163903 (2006).

30. J. Masajada, M. Leniec, E. Jankowska, H. Thienpont, H. Ottevaere, and V. Gomez, "Deep microstructure topography characterization with optical vortex interferometer," Opt. Express **16**(23), 19179–19191 (2008).

31. M. P. J. Lavery, F. C. Speirits, S. M. Barnett, and M. J. Padgett, "Detection of a Spinning Object Using Light's Orbital Angular Momentum," Science **341**(6145), 537–540 (2013).

32. X. Fang, H. Ren, and M. Gu, "Orbital angular momentum holography for high-security encryption," Nat. Photonics **14**(2), 102–108 (2020).

33. G. J. Gbur, *Singular Optics* (CRC, 2017).

34. Y. Yang, Q. Zhao, L. Liu, Y. Liu, C. Rosales-Guzmán, and C. Qiu, "Manipulation of Orbital-Angular-Momentum Spectrum Using Pinhole Plates," Phys. Rev. Appl. **12**(6), 064007 (2019).

35. X. Qiu, F. Li, W. Zhang, Z. Zhu, and L. Chen, "Spiral phase contrast imaging in nonlinear optics: seeing phase objects using invisible illumination," Optica **5**(2), 208–212 (2018).

36. X. Liu, Y. Shen, L. Liu, F. Wang, and Y. Cai, "Experimental demonstration of vortex phase-induced reduction in scintillation of a partially coherent beam," Opt. Lett. **38**(24), 5323–5326 (2013).

37. G. Gbur, T. D. Visser, and E. Wolf, "'Hidden' singularities in partially coherent wavefields," J. Opt. A: Pure Appl. Opt. **6**(5), S239–S242 (2004).

38. X. Lu, C. Zhao, Y. Shao, J. Zeng, S. Konijnenberg, X. Zhu, S. Popov, H. P. Urbach, and Y. Cai, "Phase detection of coherence singularities and determination of the topological charge of a partially coherent vortex beam," Appl. Phys. Lett. **114**(20), 201106 (2019).

39. J. Zeng, X. Lu, L. Liu, X. Zhu, C. Zhao, and Y. Cai, "Simultaneous measurement of the radial and azimuthal mode indices of a higher-order partially coherent vortex beam based on phase detection," Opt. Lett. **44**(15), 3881–3884 (2019).

40. L. Guo, Y. Chen, X. Liu, L. Liu, and Y. Cai, "Vortex phase-induced changes of the statistical properties of a partially coherent radially polarized beam," Opt. Express **24**(13), 13714–13728 (2016).

41. M. V. Berry, "Optical vortices evolving from helicoidal integer and fractional phase steps," J. Opt. A: Pure Appl. Opt. **6**(2), 259–268 (2004).

42. G. Gbur, "Fractional vortex Hilbert's Hotel," Optica **3**(3), 222–225 (2016).

43. Y. Yang, X. Zhu, J. Zeng, X. Lu, C. Zhao, and Y. Cai, "Anomalous Bessel vortex beam: modulating orbital angular momentum with propagation," Nanophotonics **7**(3), 677–682 (2018).

44. S. H. Tao, X. C. Yuan, J. Lin, X. Peng, and H. B. Niu, "Fractional optical vortex beam induced rotation of particles," Opt. Express **13**(20), 7726–7731 (2005).

45. C. S. Guo, Y. N. Yu, and Z. Hong, "Optical sorting using an array of optical vortices with fractional topological charge," Opt. Commun. **283**(9), 1889–1893 (2010).

46. G. Situ, G. Pedrini, and W. Osten, "Spiral phase filtering and orientation-selective edge detection/enhancement," J. Opt. Soc. Am. A **26**(8), 1788–1797 (2009).

47. S. S. R. Oemrawsingh, J. A. de Jong, X. Ma, A. Aiello, E. R. Eliel, G. W. 't Hooft, and J. P. Woerdman, "High-dimensional mode analyzers for spatial quantum entanglement," Phys. Rev. A **73**(3), 032339 (2006).

48. S. Li, B. Shen, X. Zhang, Z. Bu, and W. Gong, "Conservation of orbital angular momentum for high harmonic generation of fractional vortex beams," Opt. Express **26**(18), 23460–23470 (2018).

49. A. V. Volyar and Y. A. Egorov, "Super pulses of orbital angular momentum in fractional-order spiroid vortex beams," Opt. Lett. **43**(1), 74–77 (2018).

50. D. Deng, M. Lin, Y. Li, and H. Zhao, "Precision Measurement of Fractional Orbital Angular Momentum," Phys. Rev. Appl. **12**(1), 014048 (2019).

51. S. Li, B. Shen, W. Wang, Z. Bu, H. Zhang, H. Zhang, and S. Zhai, "Diffraction of relativistic vortex harmonics with fractional average orbital angular momentum," Chin. Opt. Lett. **17**(5), 050501 (2019).

52. J. Wen, L. G. Wang, X. Yang, J. Zhang, and S. Y. Zhu, "Vortex strength and beam propagation factor of fractional vortex beams," Opt. Express **27**(4), 5893–5904 (2019).

53. J. Zeng, X. Liu, F. Wang, C. Zhao, and Y. Cai, "Partially coherent fractional vortex beam," Opt. Express **26**(21), 26830–26844 (2018).

54. F. Gu, L. Li, C. Chang, C. Yuan, S. Feng, S. Nie, and J. Ding, "Generation of fractional ellipse perfect vector beams," Opt. Commun. **443**, 44–47 (2019).

55. E. Wolf, *Introduction to the Theory of Coherence and Polarization of Light* (Cambridge University, 2007).

56. L. Mandel and E. Wolf, *Optical coherence and quantum optics* (Cambridge University, 1995).
57. F. Gori, V. Ramírez-Sánchez, M. Santarsiero, and T. Shirai, "On genuine cross-spectral density matrices," J. Opt. A: Pure Appl. Opt. **11**(8), 085706 (2009).
58. V. V. Kotlyar, A. A. Kovalev, and A. V. Volyar, "Topological charge of a linear combination of optical vortices: topological competition," Opt. Express **28**(6), 8266–8281 (2020).
59. O. Korotkova and E. Wolf, "Changes in the state of polarization of a random electromagnetic beam on propagation," Opt. Commun. **246**(1-3), 35–43 (2005).
60. P. Meemon, M. Salem, K. S. Lee, M. Chopra, and J. P. Rolland, "Determination of the coherency matrix of a broadband stochastic electromagnetic light beam," J. Mod. Opt. **55**(17), 2765–2776 (2008).
61. X. Liu, T. Wu, L. Liu, C. Zhao, and Y. Cai, "Experimental determination of the azimuthal and radial mode orders of a partially coherent LGpl beam," Chin. Opt. Lett. **15**(3), 030002 (2017).
62. S. N. Khonina, V. V. Kotlyar, M. V. Shinkaryev, V. A. Soifer, and G. V. Uspleniev, "The phase rotor filter," J. Mod. Opt. **39**(5), 1147–1154 (1992).
63. P. Santis, F. Gori, G. Guattari, and C. Palma, "An example of a Collett-Wolf source," Opt. Commun. **29**(3), 256–260 (1979).
64. Y. Fang, Q. Lu, X. Wang, W. Zhang, and L. Chen, "Fractional-topological-charge-induced vortex birth and splitting of light fields on the submicron scale," Phys. Rev. A **95**(2), 023821 (2017).
65. F. Wang and Y. Cai, "Experimental observation of fractional Fourier transform for a partially coherent optical beam with Gaussian statistics," J. Opt. Soc. Am. A **24**(7), 1937–1944 (2007).